Expansion of calcium microdomains regulates fast exocytosis at a ribbon synapse

Vahri Beaumont*, Artur Llobet, and Leon Lagnado†

Medical Research Council Laboratory of Molecular Biology, Hills Road, Cambridge CB2 2QH, United Kingdom

Edited by Charles F. Stevens, The Salk Institute for Biological Studies, La Jolla, CA, and approved May 31, 2005 (received for review March 10, 2005)

We investigated the Ca^{2+} signal regulating fast exocytosis at the ribbon synapse of retinal bipolar cells by using total internal reflection fluorescence microscopy to image fluorescent Ca^{2+} indicators and interference reflection microscopy to monitor exocytosis. Depolarization generated Ca^{2+} "microdomains" that expanded over the time scale during which the rapidly releasable pool (RRP) of vesicles was released (<40 ms). Replacing mobile Ca^{2+} buffers in the terminal with 10 mM EGTA prevented expansion of microdomains and decreased the number of rapidly releasable vesicles by a factor of 2. Conversely, decreasing the concentration of EGTA in the terminal to 0.1 mM increased the apparent width of a Ca^{2+} microdomain from 580 nm to 930 nm and increased the size of the RRP size by a factor of 1.5. The $[Ca^{2+}]$ over the area that the microdomain expanded was estimated to be 2–7 μM. These results indicate that vesicles within the RRP are located hundreds of nanometers from Ca^{2+} channels, and that fusion of these vesicles can be triggered by low micromolar levels of Ca^{2+}. Variable distances between docked vesicles and Ca^{2+} channels at the active zone, therefore, provide an explanation for the heterogeneous release probability of vesicles comprising the RRP.

Communication between neurons occurs when the opening of Ca^{2+} channels in the nerve terminal triggers exocytosis of synaptic vesicles containing neurotransmitters (1, 2). A key determinant of this process is the spatial coupling between Ca^{2+} channels and vesicles in the presynaptic membrane. At the squid giant synapse, Ca^{2+} ions exert their action within a "nanodomain" extending a few tens of nanometers from the channel (3). This idea emerged from the effects of Ca^{2+} chelators: Fast exocytosis at the squid giant synapse can be inhibited by 1 mM 1,2-bis(2-aminophenoxy)ethane-*N*,*N*,*N*′,*N*′-tetraacetic acid (BAPTA) but not by EGTA at concentrations up to 80 mM (4, 5). These chelators bind Ca^{2+} ions with similar affinity, but EGTA does so ≈100-fold more slowly than BAPTA, so that 80 mM EGTA is expected to allow a free Ca^{2+} ion to travel a mean distance of ≈30 nm before capture (6, 7).

In other neurons, Ca^{2+} channels and vesicles at the active zone are coupled less closely. At concentrations of 10 mM, EGTA can substantially inhibit fast exocytosis at a number of central synapses (8–10), even though a free Ca^{2+} ion will travel a mean distance of ≈90 nm (8–10). The $[Ca^{2+}]$ at these distances from Ca^{2+} channels is expected to be <10 μM (3, 7), and release of caged Ca^{2+} has directly demonstrated that a $[Ca^{2+}]$ as low as 1 μM can drive fast exocytosis at the Calyx of Held (11, 12). The Ca^{2+} signal operating over distances where EGTA is an effective buffer has been termed the "Ca^{2+} microdomain," and this signal is generated by the synchronous opening of many channels at the active zone (13). Optical techniques have allowed Ca^{2+} microdomains to be visualized at the ribbon synapse of hair cells (14) and bipolar cells (15), the neuromuscular junction (16), and in neuroendocrine cells (17).

Capacitance measurements in retinal bipolar cells indicate that only ≈20% of the vesicles within the rapidly releasable pool (RRP) are coupled to Ca^{2+} channels tightly enough to be released in the presence of 70 mM EGTA (18). The pool of vesicles that supports fast exocytosis is heterogeneous in terms of release probability. For instance, when the amplitude of the Ca^{2+} current is reduced, only ≈40% of the RRP is released rapidly and the remainder is released slowly (19). Inhibition of fast exocytosis by "slow" Ca^{2+} buffers and heterogeneous release probability within the RRP has also been observed at the Calyx of Held (8, 20). Modeling indicates that such variability might arise if vesicles docked in and around the active zone experienced different Ca^{2+} signals because some vesicles are located very close to Ca^{2+} channels, whereas others are located further away (19–21). Unfortunately, the results of modeling studies are sensitive to properties of synapses that are incompletely understood, such as the distribution of Ca^{2+} channels, the density of Ca^{2+} pumps and their rate of operation, and the distribution of Ca^{2+}-binding proteins in and around the active zone. We therefore sought to investigate the Ca^{2+} signal triggering fast exocytosis experimentally. We used total internal reflection fluorescence microscopy (TIRFM) to image fluorescent Ca^{2+} indicators within ≈100 nm of the surface membrane at the synaptic terminal of retinal bipolar cells (15). We found that the capacity of the RRP was correlated with the spatial extent of the Ca^{2+} microdomain, with vesicles comprising the RRP lying hundreds of nanometers from the center of the active zone, where a $[Ca^{2+}]$ in the low micromolar range was sufficient to trigger fast release. These results provide direct evidence in support of the idea that heterogeneity of the RRP reflects variable distances between docked vesicles and Ca^{2+} channels at the active zone.

Materials and Methods

Electrophysiology. Depolarizing bipolar cells were isolated from the retinae of goldfish by enzymatic digestion as described in ref. 22. The external solution contained 120 mM NaCl, 2.5 mM KCl, 2.5 mM $CaCl_2$, 1 mM $MgCl_2$, 10 mM Hepes, and 10 mM glucose (pH 7.3, 280 mosM·kg^{-1}). Patch pipettes contained 110 mM cesium methane sulfonate, 10 mM TEACl, 5 mM $MgCl_2$, 3 mM Na_2ATP, 1 mM Na_2GTP, 20 mM Hepes, 0.1–0.2 mM calcium green-5N or Fluo-5F, and either 0.1 mM EGTA or 10 mM EGTA (pH 7.2 and 260 mosM·kg^{-1}). Perforated patch recordings were occasionally made with the addition of 350 $\mu g/ml^{-1}$ amphotericin B. Cells were voltage-clamped at −70 mV by using an Axopatch 200A amplifier (Axon Instruments, Union City, CA) and stimulated by depolarization to −10 mV to elicit a maximal calcium current.

Total Internal Reflection Fluorescence Microscopy. An Axiovert 100 inverted microscope (Zeiss) was modified for "through-the-objective" TIRFM by removal of the normal epifluorescence condenser (23). Illumination was provided by the 488-nm line of an Argon Ion laser coupled through a single-mode fiber. The beam was expanded 10 times and then reflected through the epifluorescence port of the microscope by a mirror at an angle of 45° that reflected the beam in parallel with the optical axis of the microscope. The beam was focused to the back focal plane of a 1.45-numerical

This paper was submitted directly (Track II) to the PNAS office.

Abbreviations: RRP, rapidly releasable pool; TIRFM, total internal reflection fluorescence microscopy; PSF, point-spread function; FWHM, full width at half maximum; CG5N, calcium green-5N; IRM, interference reflection microscopy.

*Present address: Merck Sharp and Dohme Research Laboratories, Neuroscience Research Centre, Terlings Park, Harlow, Essex CM20 2QR, United Kingdom.

†To whom correspondence should be addressed. E-mail: LL1@mrc-lmb.cam.ac.uk.

www.pnas.org/cgi/doi/10.1073/pnas.0501961102

aperture ×60 oil-immersion objective (Olympus, Melville, NY) by means of a convex lens (focal length = 400 mm). Translation of the mirror altered the radial position of the laser beam in the back focal plane of the objective and, therefore, the angle at which it left the objective. Positioning the beam at the periphery of the objective caused it to suffer total internal reflection at the interface between the coverslip and aqueous medium. The angle of incidence at the surface of the coverslip was measured as 70.4° by using a glass hemicylinder, indicating the characteristic penetration depth of the evanescent field to be 107 nm (assuming a cell refractive index of 1.38).

The filter block in the microscope was equipped with a dichroic mirror (505DRLP, Omega Optical, Brattleboro, VT) and contaminating light from the laser was removed by using a holographic notch filter (Thermo Oriel, Stratford, CT). Images were magnified ×3 by a telescope focused onto the intensifier of a charge-coupled device camera (PentaMAX, Roper Scientific, Trenton, NJ). Each pixel corresponded to an area of 125 × 125 nm in the object plane. Images were acquired at 20–50 Hz and saved by using WINVIEW32 V.2.5.A software (Roper Scientific). Acquisition of electrophysiological signals and images were time-locked by triggering from a pulse generator (Master-8, AMPI). Image analysis was performed by using IPLAB V.3.5.5 (Scanalytics, Fairfax, VA) and IGOR PRO (WaveMetrics, Lake Oswego, OR).

To estimate the point-spread function (PSF) of the microscope, we imaged fluorescent latex beads 100 nm in diameter (TetraSpek, Molecular Probes). Intensity profiles through beads exhibited a full width at half maximum (FWHM) of 400 nm and a shape that could be described as the sum of two Gaussians distributions (see Fig. 5*B*).

Fluorescent Calcium Indicators. Calibration of calcium green-5N (CG5N) was performed under TIRFM illumination by using buffered solutions containing 20 μM CG5N and a free [Ca^{2+}] of 0–1 mM (Molecular Probes). CG5N displayed a F_{max}/F_{min} of 5.8 with an apparent K_d of 14.7 μM. For Fluo-5F, F_{max}/F_{min} was 64 and we assumed an apparent K_d of 2.3 μM (Molecular Probes). Conversion of CG5N and Fluo-5F signals to free [Ca^{2+}] were calculated as $[Ca^{2+}] = K_d [(F - F_{min})/(F_{max} - F)]$, with the assumption that $F_{rest} = F_{min}$. The resting free [Ca^{2+}] in bipolar cell terminals is ≈50 nM (22), so this approximation is more accurate for CG5N (K_d = 14.7 μM) than Fluo-5F (K_d = 2.3 μM).

Interference Reflection Microscopy (IRM). An inverted epifluorescence microscope (Zeiss Axiovert 135M) was used with a half-silvered mirror in the filter block, as described in ref. 24. Illumination was provided by white light from a tungsten filament lamp, and imaging was performed with a 1.4-numerical aperture ×63 objective. The image was magnified 2-fold with a telescope placed between the microscope and the charge-coupled device camera (4910 series, Cohu, San Diego). Contrast and gain were altered using an Argus 10 image processor (Hamamatsu, Bridgewater, NJ), and the video signals were digitized by an LG-3 board (Scion, Frederick, MD) driven by NIH IMAGE software (http://rsb.info.nih.gov/nih-image). The area of the bipolar terminal footprints was measured in NIH IMAGE or IMAGEJ software (http://rsb.info.nih.gov/ij) by using macros that operated on the raw movie associated with a single stimulus. These movies were acquired with 8-bit resolution. To determine area increases during depolarization, the first video frame in the sequence was thresholded to define the footprint but reject the surround. Next, all of the pixels in the largest contiguous region defined by this threshold were counted. The same threshold value was used for the area measurement in all frames of a stimulus movie. To visualize the change in the area of the footprint, "difference movies" were made by averaging 25 video frames from the beginning of a sequence and subtracting this "resting" image from all of the individual frames in the sequence (24). Difference movies were made by converting the raw 8-bit movies to 64-bit floating point, thereby allowing pixels to have negative as well as positive values. In a difference movie, areas of no change appear gray with pixel values of zero, whereas areas where the footprint expands appear darker with negative pixel values.

All results, including those plotted on graphs, are expressed as mean ± SEM.

Results

Exocytosis Under Different Conditions of Calcium Buffering. We used IRM to measure changes in membrane surface area caused by exocytosis in the region of the synaptic terminal closely attached to the glass coverslip (the "footprint"). Previous studies have used the capacitance technique to monitor exocytosis in retinal bipolar cells (25, 26); the advantage of IRM is that it provides a quantitative measure of exocytosis throughout a single depolarizing stimulus, allowing immediate measurement of fast and slow phases of release (see ref. 24 and *Supporting Text*, which is published on the PNAS web site). Fig. 1*A* and Movie 1, which is published as supporting information on the PNAS web site, show an individual IRM response elicited by a depolarization lasting 500 ms, and Fig. 1 *B* and *C* shows the averaged time course of the change in area of the footprint under different conditions of Ca^{2+} buffering. The fastest phase of expansion, representing release of the RRP, was equivalent to 1.2 ± 0.1% of the surface area when the perforated patch technique was used to preserve mobile Ca^{2+} buffers in the terminal (red trace). The reserve pool of vesicles was released at a rate of 3.6% of the surface area per second.

The kinetics of exocytosis were altered by whole-cell dialysis with patch pipettes containing 10 mM EGTA; the capacity of the RRP was halved to 0.6% of the surface area, and release of the reserve pool of vesicles was reduced to 1.6% of the surface area per second (Fig. 1*C*, black trace). In contrast, dialysis with 0.1 mM EGTA caused the RRP to increase to 1.8% of the surface area, a factor of 1.5 relative to its capacity in the presence of endogenous Ca^{2+} buffers. Under these conditions of weak buffering, release of the reserve pool of vesicles was accelerated to 6.1% of the surface area per second (blue trace). The fast and slow phases of exocytosis supported by the RRP and reserve pool of vesicles were therefore both sensitive to EGTA, indicating that the majority of vesicles in this terminal were not tightly coupled to Ca^{2+} channels (18). In all conditions, the fast phase of exocytosis was complete within 40 ms. Increasing the Ca^{2+}-buffering capacity of the cytoplasm also slowed down the rate of endocytosis (Fig. 1*B*), in agreement with a previous study using the capacitance technique (27).

Visualization of Calcium Microdomains. To visualize Ca^{2+} signals at the active zone under these different conditions of Ca^{2+} buffering, we used TIRFM in conjunction with fluorescent Ca^{2+} dyes. Zenisek and colleagues (15) have shown that areas of Ca^{2+} influx correspond with the ribbons that are a defining feature of the active zone in bipolar cells (see also *Supporting Text*). In Fig. 6 and Movie 2, which are published as supporting information on the PNAS web site, we also show that Ca^{2+} influx occurs in areas of membrane expansion following exocytosis. We used CG5N as a Ca^{2+} indicator because the relatively low affinity of this dye (K_d = 14.7 μM) allowed us to visualize local Ca^{2+} signals under conditions of low Ca^{2+} buffering as well as high. The example in Fig. 2 *A* and *B* shows a footprint in which three localized sources of Ca^{2+} influx were observed, each representing Ca^{2+} channels held in a tight cluster. These calcium microdomains were generated by a 500-ms depolarization through a whole-cell pipette containing 10 mM EGTA and 100 μM CG5N. The center of Ca^{2+} influx was defined by averaging the 25 images showing the relative change in fluorescence ($\Delta F/F$) recorded during depolarization, then locating the pixel in which the signal was brightest. The spatial extent of an individual microdomain was then obtained by averaging the profiles along lines placed horizontally and vertically through the center. The

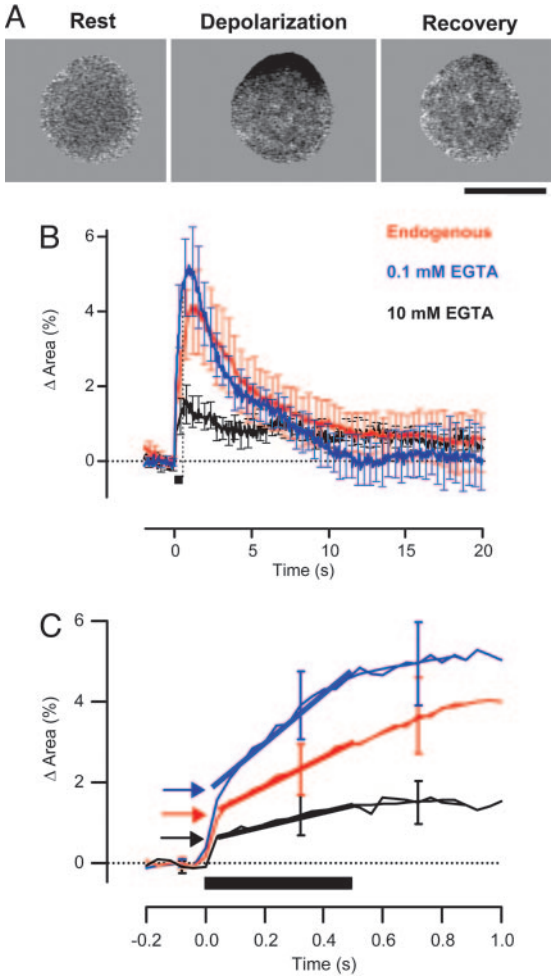

Fig. 1. Exocytosis of the RRP and reserve pool of vesicles under different conditions of Ca^{2+} buffering. (*A*) Expansion of the footprint in response to a 500-ms depolarization imaged by IRM. The footprint is shown at rest, at the end of the stimulus period and 15 s after the stimulus. The dark area represents the region of increased destructive interference because of membrane expansion onto the coverslip (see also Movie 1 and *Supporting Text* for more detail on IRM). This recording was made in the perforated patch configuration. (Scale bar: 5 μm.) (*B*) Expansion of the footprint was measured by IRM under the following conditions of Ca^{2+} buffering: endogenous buffers (red trace, $n = 12$), 10 mM EGTA (black, $n = 7$), and 0.1 mM EGTA (blue, $n = 8$). The change in the area of the footprint is expressed as a percentage of the area at rest to allow a quantitative comparison with previous measurements made by using the capacitance technique and FM1–43. The timing of the depolarization is indicated by the black bar. (*C*) Expansion of the traces in *B*, to show the distinct kinetic phases of exocytosis. Release of the reserve pool of vesicles occurred at a relatively constant rate, which was measured by fitting traces with a straight line (shown by heavy lines). The size of the RRP was estimated by extrapolating this line back to the beginning of the stimulus (arrows). The rate of asynchronous release was estimated by fitting a straight line to the trace over the 300-ms period after the stimulus (thin lines). In the presence of endogenous buffers, release of the reserve pool was little affected by closure of Ca^{2+} channels.

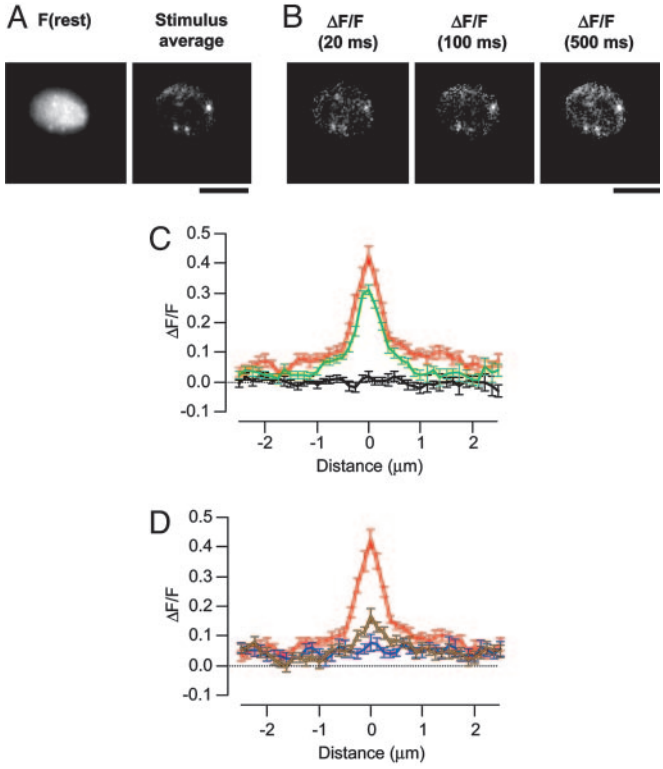

Fig. 2. Stationary microdomains in the presence of 10 mM EGTA. (*A*) Image of a footprint at rest, and $\Delta F/F$ averaged during a 500-ms depolarization. At least three distinct clusters of Ca^{2+} channels were observed, each colocalizing with a punctum of CG5N observed at rest. (Scale bar: 5 μm.) See also Movie 3. (*B*) Individual frames showing $\Delta F/F$ at the times indicated relative to the onset of the stimulus. (*C*) Averaged profile of $\Delta F/F$, through Ca^{2+} microdomains at rest (black) and 20 ms (green) and 500 ms (red) after the onset of the stimulus. Average of 25 microdomains from ten footprints. (*D*) Profile through Ca^{2+} microdomains at the end of a 500 ms depolarization (red), and then 20 ms (brown) and 40 ms (blue) after closure of Ca^{2+} channels. Note that local Ca^{2+} gradients collapsed completely within 20 to 40 ms.

averaged profiles of the Ca^{2+} signal at different times during and after a depolarization in 10 mM EGTA are shown in Fig. 2 *C* and *D* (25 microdomains and 10 different terminals). The spatial extent of the Ca^{2+} microdomain barely altered during the 500-ms period of Ca^{2+} influx (Movie 3, which is published as supporting information on the PNAS web site), and microdomains collapsed within 20 to 40 ms after the closure of Ca^{2+} channels (Fig. 2*D*).

Calcium microdomains could also be distinguished when the concentration of EGTA was reduced to 0.1 mM, as shown in Fig. 3 *A* and *B* and Movie 4, which is published as supporting information on the PNAS web site. The Ca^{2+} signal was localized over the first 20 ms of the depolarization (Fig. 3*C*, green trace), but over the next 20 ms a shallow gradient of Ca^{2+} began to extend from the active zone (blue trace). As Ca^{2+} influx and diffusion continued, the "global" Ca^{2+} signal became spatially uniform and the microdomain appeared to ride on top (red trace). Notably, the peak amplitude of the signal reported by CG5N did not increase even as Ca^{2+} accumulated under regions of the membrane some distance from the source of influx. The Ca^{2+} signal therefore displayed two components: localized microdomains that stabilized within 20 to 40 ms of depolarization and then collapsed within 20 to 40 ms of closing Ca^{2+} channels, and slower global Ca^{2+} rises reflecting diffusion of Ca^{2+} from these sites (15).

Calcium Microdomains and Release of the RRP. What was the nature of the calcium signal determining the fastest phase of release? The RRP was released within 20 to 40 ms of the onset of depolarization (Fig. 1), so we began by estimating the area over which the Ca^{2+} signal spread during this period. In 10 mM EGTA, the FWHM of a microdomain averaged 580 ± 40 nm in the first 20 ms of depolarization ($n = 12$; Fig. 4*A*). Microdomains in 0.1 mM EGTA were significantly wider, extending 930 ± 110 nm over the first 20 ms ($n = 12$). Comparison of these Ca^{2+} signals with exocytic responses observed under IRM (Fig. 1) demonstrated that the maintenance of a localized Ca^{2+} microdomain in 10 mM EGTA

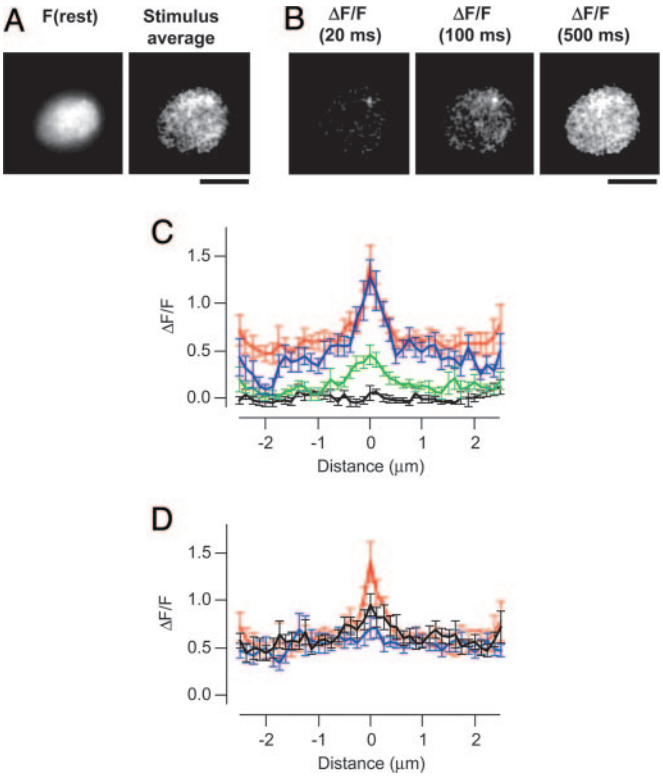

Fig. 3. Evolving microdomains in the presence of 0.1 mM EGTA. (*A*) Image of a footprint at rest, and $\Delta F/F$ averaged during a 500-ms depolarization. One cluster of Ca^{2+} channels was observed. (Scale bar: 5 μm.) See also Movie 4. (*B*) Individual frames showing $\Delta F/F$ at the times indicated relative to the onset of the stimulus. (*C*) Averaged profile of $\Delta F/F$ through Ca^{2+} microdomains at rest (black) and 20 ms (green), 40 ms (blue), and 500 ms (red) after the onset of the stimulus. The spread of Ca^{2+} beyond the area of influx was obvious within 40 ms. After 500 ms of Ca^{2+} influx, the microdomain appeared to ride on top of a spatially uniform rise in Ca^{2+}. Results are an average of 12 microdomains from 8 footprints. (*D*) Profile through Ca^{2+} microdomains at the end of a 500-ms depolarization (red), and then 20 ms (black) and 40 ms (blue) after closure of Ca^{2+} channels. Note that local Ca^{2+} gradients collapsed completely within 20 to 40 ms.

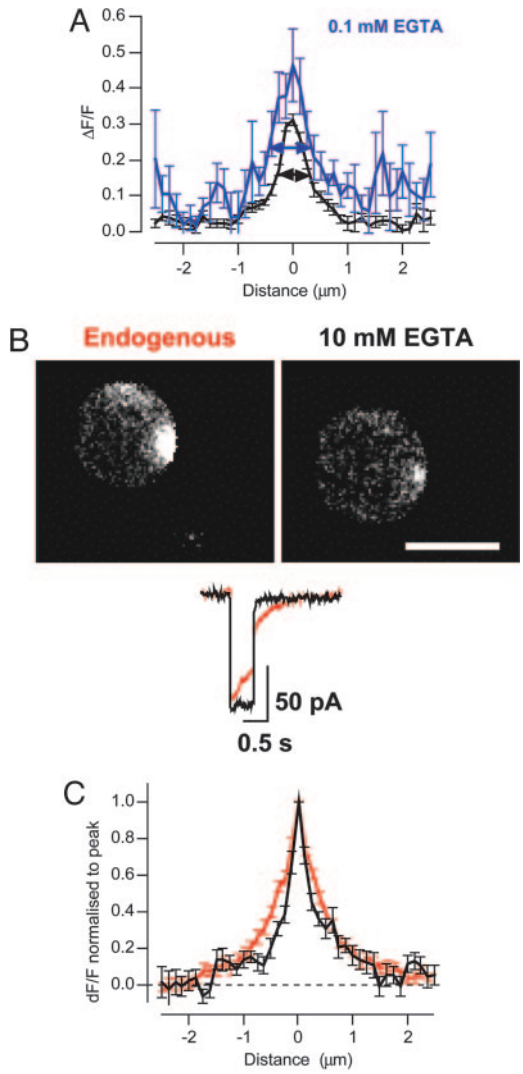

Fig. 4. The spatial extent of Ca^{2+} microdomains related to the size of the RRP. (*A*) Comparison of the profile of $\Delta F/F$, although Ca^{2+} microdomains imaged over the first 20 ms of Ca^{2+} influx in 0.1 mM (blue) and 10 mM EGTA (black). The width of the microdomain was measured as FWHM (arrowed lines). (*B*) Individual frames showing $\Delta F/F$ 20 ms after the onset of depolarization in the presence of endogenous Ca^{2+} buffers, and then after rupture of the patch to introduce 10 mM EGTA. These measurements were made by using Fluo-5F. (Scale bar: 5 μm.) The peak calcium current was not significantly altered after patch rupture. (*C*) Profile of $\Delta F/F$ through Ca^{2+} microdomains imaged over the first 20 ms of Ca^{2+} influx. FWHM was 770 $\pm$ 60 nm under endogenous buffer conditions (red) and 450 $\pm$ 50 nm after dialysis with 10 mM EGTA (black; 17 microdomains from 10 footprints).

prevented fast release of $\approx$70% of vesicles that were available for fast exocytosis in 0.1 mM EGTA. Preventing expansion of the microdomain also strongly inhibited release of the reserve pool of vesicles. The amplitude of the microdomain above the global Ca^{2+} signal was not significantly different in either buffer condition: peak $\Delta F/F$ was 0.22 $\pm$ 0.02 in 10 mM EGTA (n = 25) and 0.28 $\pm$ 0.03 in 0.1 mM EGTA (n = 11). These results indicate that the majority of vesicles with the potential for fast release were located hundreds of nanometers from Ca^{2+} channels at the active zone.

What of microdomains under normal conditions of Ca^{2+} buffering? To prevent loss of mobile Ca^{2+} buffers normally present in bipolar cells, measurements were made by using the perforated patch technique (18). Attempts to load bipolar cells with the acetoxymethyl (AM) ester of CG5N were unsuccessful, so we used the AM ester of Fluo-5F (K_d = 2.3 μM). After the microdomain was visualized in the presence of endogenous buffers, the patch was ruptured to introduce 10 mM EGTA and 100 μM Fluo-5F and the measurement was repeated. In all cases, the fluorescence of Fluo-5F was either unaltered or modestly increased after membrane rupture, indicating that AM-loading of the dye had resulted in an intracellular Fluo-5F concentration of <100 μM. Microdomains that were relatively wide under normal conditions became more restricted in the presence of 10 mM EGTA (Fig. 4 *B* and *C*). Microdomains observed over the first 20 ms displayed a FWHM of 770 $\pm$ 60 nm (n = 13) in the presence of endogenous Ca^{2+} buffers that was reduced to 450 $\pm$ 50 nm in 10 mM EGTA (Fig. 4*C*). Comparison with the exocytic responses measured under IRM (Fig. 1) again demonstrated that a wider microdomain was correlated with a larger RRP.

The Calcium Signal Around the Active Zone. By using an evanescent field that decayed with a length-constant of $\approx$100 nm, in combination with a low-affinity Ca^{2+} indicator, it was possible to visualize the accumulation of free Ca^{2+} ions in the vicinity of the active zone. The red and blue traces in Fig. 5*A* compare the Ca^{2+} profiles in the first and second 20-ms periods of Ca^{2+} influx in 0.1 mM EGTA; the frame integrating light over the period 20–40 ms from the start of Ca^{2+} influx demonstrates an obvious accumulation of Ca^{2+} at

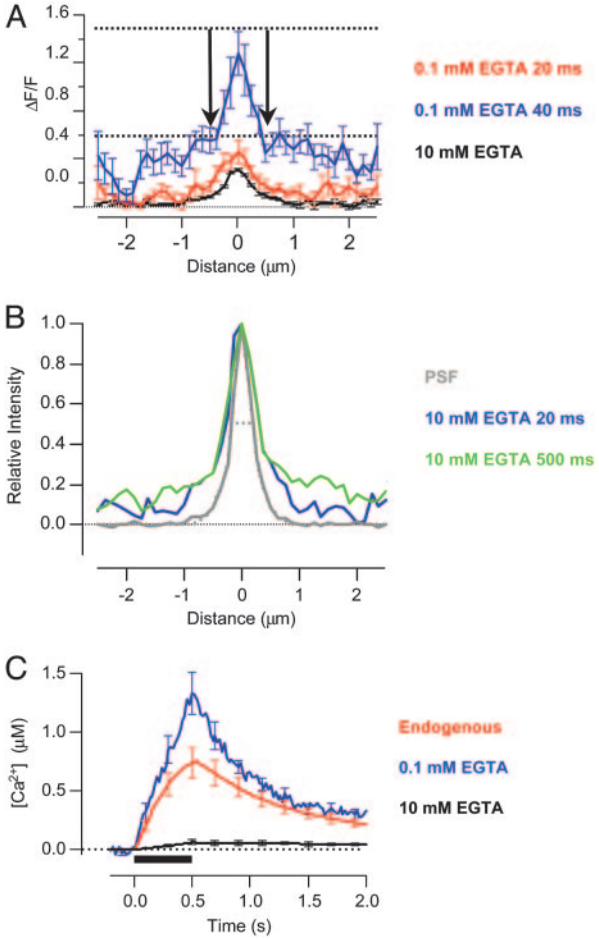

Fig. 5. Calcium signal governing fast and slow exocytosis. (*A*) Microdomain profiles measured by using CG5N at 20 ms (red) and 40 ms (blue) from the beginning of depolarization in 0.1 mM EGTA. The accumulation of Ca^{2+} beyond the source of influx was obvious at distances of a few hundred nanometers. The shallow gradient of Ca^{2+} around the periphery generated a maximum value of $\Delta F/F$ of ≈0.6 (lower dashed line). The stationary microdomain in 10 mM EGTA is also shown for comparison (black trace from *B*, after a 500-ms depolarization). Over the period that the RRP was released, the maximum value of $\Delta F/F$ in 0.1 mM EGTA did not exceed 1.5, placing an upper limit on the signal arising from spread of Ca^{2+} beyond this stationary microdomain. (*B*) Averaged intensity profile through a fluorescent bead 100 nm in diameter, providing a measure of the PSF of our microscope (gray). The dashed line fitted to the measurements is the sum of two Gaussians with standard deviations of 112 nm and 518 nm and relative amplitudes of 0.71:1. The PSF is also compared with the normalized profiles of the microdomains (CG5N) in 10 mM EGTA at 20 ms (blue) and 500 ms (green) from the beginning of depolarization. The profiles deviated from the PSF beyond a few hundred nanometers from the center, indicating a small accumulation of Ca^{2+} at these distances. (*C*) The increase in free $[Ca^{2+}]$ in response to a depolarization lasting 500 ms (bar) was measured in endogenous buffer conditions (red, using Fluo-5F), 10 mM EGTA (black, using Fluo-5F), and 0.1 mM EGTA (blue, using CG5N). Measurements were made in a region of interest covering 1.6 μm^2 remote from microdomains.

distances as short as 500 nm from the center of the cluster of Ca^{2+} channels, as shown by the bold arrows (see also Fig. 3*C*). This accumulation of Ca^{2+} overlapped in time with release of the RRP, which took 20–40 ms to be complete in the presence of 0.1 mM EGTA (Fig. 1). The Ca^{2+} gradient was not an artifact caused by the blurring of images by the PSF of the microscope because it was not nearly as clear in the frame integrating light over the period 0–20 ms from the start of Ca^{2+} influx and because it was substantially reduced in 10 mM EGTA. Even the stationary Ca^{2+} profiles in 10 mM EGTA exhibited a "shoulder" beyond the central peak that was not observed in the PSF (Fig. 5*B*), indicating a shallow gradient of Ca^{2+} extending from the central cluster of Ca^{2+} channels. Complete release of the RRP occurred over a period of 20–40 ms in the presence of 0.1 mM EGTA, so these observations indicate that accumulation of Ca^{2+} across the active zone and immediate surrounding area was correlated with a larger RRP (Fig. 1).

The gradients surrounding open Ca^{2+} channels have been modeled by using analytical methods and numerical simulations (7, 21, 28). One useful approach to understanding these gradients is the "rapid buffer approximation," which assumes that the buffers are so fast that they will be in equilibrium with Ca^{2+} in space and time (6, 29). This condition is most likely to hold true at distances >100 nm from a Ca^{2+} channel and on time scales >1 ms (7). The rapid buffer approximation is therefore useful during the evolution of the Ca^{2+} signals detected by CG5N because the reaction time constant of 100 μM CG5N binding Ca^{2+} (K_{on} = 130 $\mu M^{-1} \cdot s^{-1}$, ref. 30) is expected to be ≈70 μs, which is much shorter than the 20- to 40-ms time scale over which the RRP is released (18). We therefore used the equilibrium equation of CG5N to obtain an estimate of the Ca^{2+} concentration averaged over the region that the microdomain was seen to expand (i.e., the immediate margins of the central peak indicated by the arrows in Fig. 5*A*). The relative change in fluorescence of CG5N in this area was ≈0.6 over the period 20–40 ms from the beginning of the stimulus. A value of 0.6 for $\Delta F/F$ converts to an increase in free $[Ca^{2+}]$ of ≈2 μM. A second, simpler approach was to measure $\Delta F/F$ right at the peak of the microdomain; the value was 1.5 (upper dashed line in Fig. 5*A*), which converts to a free $[Ca^{2+}]$ of ≈7 μM. This second method of estimation provides an upper limit to the spatially averaged free $[Ca^{2+}]$ over the area that the microdomain expanded (i.e., shallow gradient in the blue trace) and does not depend on assumptions about the rate at which the Ca^{2+} gradient evolves. These results indicate that a $[Ca^{2+}]$ of a few micromolars was sufficient to drive fast release of vesicles a few hundred nanometers from the center of the active zone.

The Global Ca Signal and Release of the Reserve Pool of Vesicles. Calcium microdomains regulated fast release of the RRP, but did they also affect slower release of the reserve pool of vesicles? When the mobile Ca^{2+} buffers within the terminal were maintained under perforated patch, the reserve pool was released at a rate equivalent to 3.6 ± 0.1% of the resting surface area per second while Ca^{2+} channels were open, and at a rate of 3.5 ± 0.2% per second for a further 300 ms after Ca^{2+} channels were closed (Fig. 1 *B* and *C*, red trace, and Table 1). Calcium microdomains collapsed within 20 ms of closure of Ca^{2+} channels (Figs. 2 and 3), indicating that release of the reserve pool of vesicles was not driven by the Ca^{2+} signal close to open Ca^{2+} channels but by the global Ca^{2+} signal resulting from diffusion under the membrane. We therefore estimated the $[Ca^{2+}]$ over areas of the footprint remote from Ca^{2+} microdomains. In 10 mM EGTA, the submembranous $[Ca^{2+}]$ did not rise by >60 nM during the course of the depolarization (0.062 ± 0.02 μM; n = 11; Fig. 5*C*), whereas in 0.1 mM EGTA it rose to a peak of 1.4 ± 0.2 μM (n = 12), and in endogenous buffering conditions it rose to 0.75 ± 0.13 μM (n = 12). Increasing the global $[Ca^{2+}]$ over the micromolar range was therefore associated with an almost 4-fold increase in the rate at which the reserve pool of vesicles was released (Fig. 1 and Table 1).

Discussion

Using total internal reflection fluorescence microscopy, we were able to image Ca^{2+} microdomains under conditions that alter the kinetics of exocytosis in retinal bipolar cells. We provide evidence that the size of the RRP depends on the spatial extent of the Ca^{2+} signal at the active zone, with $[Ca^{2+}]$ in the low micromolar range triggering fast release of vesicles at distances up to hundreds of nanometers from the central region of Ca^{2+} influx. About 20% of vesicles in the RRP can still be released rapidly in the presence of

Table 1. Exocytosis and the submembranous Ca^{2+} signal

Parameter	Endogenous buffers	10 mM EGTA	0.1 mM EGTA
Rate of release of reserve pool (% surface area s^{-1})	3.6 ± 0.1	1.6 ± 0.1	6.1 ± 0.4
Rate of asynchronous release (% surface area s^{-1})	3.5 ± 0.2	0.4 ± 0.4	1.7 ± 0.4
Size of RRP (% surface area)	1.2 ± 0.1	0.6 ± 0.02	1.8 ± 0.1
Width of microdomain measured using CG5N (nm)	—	580 ± 40	930 ± 110*
Width of microdomain measured using Fluo-5F (nm)	770 ± 60*	450 ± 50	—
Peak global [Ca^{2+}] (μM)	0.75 ± 0.13	0.06 ± 0.02	1.4 ± 0.2

*Microdomain was significantly wider than that measured in 10 mM EGTA at the level of $P = 0.05$ (*t* test). Results are expressed as mean ± S.E.M.

70 mM EGTA (18), indicating that these vesicles are docked within the cluster of Ca^{2+} channels at the active zone. Variable coupling between Ca^{2+} channels and vesicles with the potential for fast release provides a simple explanation for the heterogeneous probability of release from the RRP (18, 19).

The most reliable estimate of the area over which Ca^{2+} channels cluster at a ribbon synapse has been provided by electron microscopy of saccular hair cells, where Ca^{2+} and K_{Ca} channels form "particle arrays" immediately under the ribbon covering an area ≈200 nm across (31). At this active zone, about half of the vesicles were docked towards the center, whereas the remainder (termed "outliers") were docked at the periphery, just beyond the area where the ribbon associates with the surface membrane. Vesicles at the active zone of bipolar cells also dock over an area up to 500 nm across (18, 32). The idea that a proportion of vesicles at ribbon synapses dock hundreds of nanometers from Ca^{2+} channels is also consistent with theory indicating that 0.1 mM EGTA will allow free Ca^{2+} ions to travel 1 nm from channels before capture by the chelator (7). Simulations of exocytosis at the Calyx of Held suggest that this terminal also contains vesicles that fuse at membrane sites located 30–300 nm from Ca^{2+} channels (21).

It is often suggested that the Ca^{2+} signal within tens of nanometers of Ca^{2+} channels (the "nanodomain") is the most relevant to understanding fast exocytosis at the ribbon synapse of bipolar cells (3, 11, 13, 33, 34), but the results we have presented indicate that release of the RRP is primarily controlled by microdomains. Exocytosis of the RRP was affected by a slow Ca^{2+} buffer, EGTA, which is only expected to be effective at distances of hundreds of nanometers from Ca^{2+} channels (Fig. 1). Direct visualization of the Ca^{2+} signal at the active zone also demonstrated that the size of the RRP correlated with the spatial extent of the Ca^{2+} signal around the cluster of Ca^{2+} channels (Figs. 2–5), and we estimate that the [Ca^{2+}] in this region rose to 2–7 μM (5). A submembranous [Ca^{2+}] of ≈1 μM drove release of the reserve pool of vesicles as well asynchronous release. At the Calyx of Held, fast exocytosis can also be driven by Ca^{2+} levels as low as 1–10 μM Ca^{2+} (11, 12).

It seems likely that the reserve pool of vesicles corresponds with those attached to the ribbon behind the active zone. The capacity of the reserve pool is ≈3–4 times that of the RRP (24, 26), and electron micrographs indicate that ≈3–4 times as many vesicles are attached to the ribbon as are docked to the membrane immediately beneath zone (32, 35). Imaging of individual vesicles by TIRFM indicates that ≈70% of those released during the second phase of exocytosis fuse at the active zone after transfer from a structure that was holding them immediately behind (36). Relating these observations to the present results suggests that the transfer and release of vesicles on the ribbon could be driven by a [Ca^{2+}] of 1 μM or less. The visualization of Ca^{2+} signals at the active zone may now allow the study of other processes regulated by calcium, such as fast endocytosis (27).

1. Katz, B. & Miledi, R. (1967) *Nature* **215,** 651.
2. Miledi, R. (1973) *Proc. R. Soc. London Ser. B* **183,** 421–425.
3. Augustine, G. J. (2001) *Curr. Opin. Neurobiol.* **11,** 320–326.
4. Adler, E. M., Augustine, G. J., Duffy, S. N. & Charlton, M. P. (1991) *J. Neurosci.* **11,** 1496–1507.
5. Augustine, G. J., Adler, E. M. & Charlton, M. P. (1991) *Ann. N.Y. Acad. Sci.* **635,** 365–381.
6. Naraghi, M. & Neher, E. (1997) *J. Neurosci.* **17,** 6961–6973.
7. Neher, E. (1998) *Cell Calcium* **24,** 345–357.
8. Borst, J. G. & Sakmann, B. (1996) *Nature* **383,** 431–434.
9. Ohana, O. & Sakmann, B. (1998) *J. Physiol.* **513,** 135–148.
10. Chen, C. & Regehr, W. G. (1999) *J. Neurosci.* **19,** 6257–6266.
11. Schneggenburger, R. & Neher, E. (2000) *Nature* **406,** 889–893.
12. Bollmann, J. H., Sakmann, B. & Borst, J. G. (2000) *Science* **289,** 953–957.
13. Augustine, G. J., Santamaria, F. & Tanaka, K. (2003) *Neuron* **40,** 331–346.
14. Tucker, T. & Fettiplace, R. (1995) *Neuron* **15,** 1323–1335.
15. Zenisek, D., Davila, V., Wan, L. & Almers, W. (2003) *J. Neurosci.* **23,** 2538–2548.
16. DiGregorio, D. A., Peskoff, A. & Vergara, J. L. (1999) *J. Neurosci.* **19,** 7846–7859.
17. Becherer, U., Moser, T., Stuhmer, W. & Oheim, M. (2003) *Nat. Neurosci.* **6,** 846–853.
18. Burrone, J., Neves, G., Gomis, A., Cooke, A. & Lagnado, L. (2002) *Neuron* **33,** 101–112.
19. Burrone, J. & Lagnado, L. (2000) *J. Neurosci.* **20,** 568–578.
20. Sakaba, T. & Neher, E. (2001) *J. Neurosci.* **21,** 462–476.
21. Meinrenken, C. J., Borst, J. G. & Sakmann, B. (2002) *J. Neurosci.* **22,** 1648–1667.
22. Burrone, J. & Lagnado, L. (1997) *J. Physiol.* **505,** 571–584.
23. Axelrod, D. (2001) *Traffic* **2,** 764–774.
24. Llobet, A., Beaumont, V. & Lagnado, L. (2003) *Neuron* **40,** 1075–1086.
25. Mennerick, S. & Matthews, G. (1996) *Neuron* **17,** 1241–1249.
26. Neves, G. & Lagnado, L. (1999) *J. Physiol.* **515,** 181–202.
27. Neves, G., Gomis, A. & Lagnado, L. (2001) *Proc. Natl. Acad. Sci. USA* **98,** 15282–15287.
28. Roberts, W. M. (1994) *J. Neurosci.* **14,** 3246–3262.
29. Smith, G. D., Wagner, J. & Keizer, J. (1996) *Biophys. J.* **70,** 2527–2539.
30. Escobar, A. L., Velez, P., Kim, A. M., Cifuentes, F., Fill, M. & Vergara, J. L. (1997) *Pflügers Arch.* **434,** 615–631.
31. Roberts, W. M., Jacobs, R. A. & Hudspeth, A. J. (1990) *J. Neurosci.* **10,** 3664–3684.
32. Holt, M., Cooke, A., Neef, A. & Lagnado, L. (2004) *Curr. Biol.* **14,** 173–183.
33. Matthews, G. (2000) *Nature* **406,** 835–836.
34. Fisher, T. E. & Bourque, C. W. (2001) *Prog. Biophys. Mol. Biol.* **77,** 269–303.
35. von Gersdorff, H., Vardi, E., Matthews, G. & Sterling, P. (1996) *Neuron* **16,** 1221–1227.
36. Zenisek, D., Steyer, J. A. & Almers, W. (2000) *Nature* **406,** 849–854.